

Numerical Simulation of Fluid-Structure Interaction in Human Phonation

Martin Larsson* and Bernhard Müller

Department of Energy and Process Engineering, Faculty of Engineering Science
The Norwegian University of Science and Technology
e-mail: martin.larsson@ntnu.no, bernhard.muller@ntnu.no

Summary Fluid-structure interaction in a simplified two-dimensional model of the larynx is considered to study human phonation. The flow is driven by an imposed pressure gradient across the glottis and interacts with the moving vocal folds in a self-sustained oscillation. The flow is computed by solving the 2D compressible Navier–Stokes equations using a high order finite difference method, which has been constructed to be strictly stable for linear hyperbolic and parabolic problems. The motion of the vocal folds is obtained by integrating the elastodynamic equations with a neo-Hookean constitutive model. Fluid and structure interact in a two-way coupling using a similar high order difference method. In each time step at the fluid-structure interface, the structure provides the fluid with new no-slip boundary conditions and new grid velocities, and the fluid provides the structure with new traction boundary conditions. The frequency obtained in our simulation is close to values observed in human phonation.

Introduction

Fluid-structure interaction (FSI) occurs when a flexible structure interacts with a fluid. The fluid flow exerts a stress on the structure which causes it to deform and thereby generate a new geometry for the fluid flow. This interaction is responsible for a wide range of phenomena which are crucial in engineering applications such as aircraft design and bridge construction, where structural motion is undesirable. The coupling between fluid flow and structural motion also plays an important role in many biological systems such as the cardiovascular and respiratory systems. The pulsatile blood flow in viscoelastic arteries and the transient airflow in the upper airways are the prime examples. Numerically simulating FSI in such systems can help to better understand the underlying biological mechanisms and potentially advance medical treatments [7].

A direct consequence of FSI in the vocal tract is voice generation, where the motion of the soft tissue of the vocal folds (cf. fig. 1) interacts dynamically with the glottal airflow to produce sound. The self-sustained oscillation of the vocal folds can be explained by the Bernoulli principle which states that in the absence of gravity for inviscid incompressible steady flow, the velocity v , pressure p and density ρ are related by $p + \rho v^2/2 = \text{const}$. The vocal folds being closed in their equilibrium position, initially at rest, are forced apart by the increasing lung pressure. As the air starts flowing, the velocity in the glottis increases and thus the pressure must decrease according to the Bernoulli principle. The pressure drop together with restoring elastic forces results in a closure of the vocal folds and a build-up of pressure. This cycle then repeats itself, driven only by the lung pressure. The computational challenge in aeroelastic simulations lies in dealing with unsteady flows at high Reynolds numbers, large deformations, moving interfaces, fluid-structure interaction and intrinsically 3D motion [7].

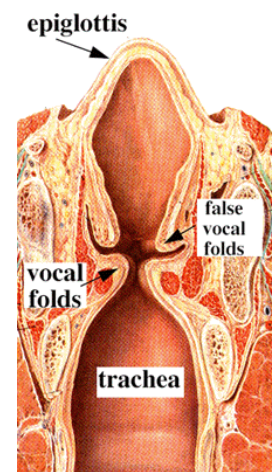


Figure 1: Cross section of larynx.

Fluid-structure interaction modelling

When solving FSI problems one has to consider the two-way coupling between the distinct physical models, i.e. fluid and structural mechanics. This can be accomplished in two ways: either *direct* or *sequential* multidisciplinary approaches. In the direct coupled field analysis approach, one solves for all the degrees of freedom of the system in one single sweep, whereas in the sequential coupling approach, the results of one solver iteration (e.g. fluid motion) is passed on as loads (traction) to the next one. Treating the flow and structural equations as one monolithic system (*direct* coupling) seems like an attractive approach from a modeling point of view. In doing so, however, one has to sacrifice efficiency and restrict to smaller-scale aeroelastic problems [35]. Historically, solution techniques for the different physical fields have evolved separately and naturally one seeks to make use of the matured techniques already available in the separate fields. Therefore, sequential coupling procedures are usually preferred, since they do not require a dedicated code [5].

Numerical models of phonation with fluid-structure interaction

The vibratory properties of the vocal folds are mainly attributed to the *lamina propria* (cf. figure 2) which is the main constituent in the mucous membranes that line various tubes in the body, particularly in the vocal tract. The lamina propria by itself is a thin layer of loose connective tissues which together with the epithelium constitute the mucosa. The functional layers of the vocal fold, with respect to phonation, can be divided into the vocal fold cover (mucosa) and the vocal fold ligament.

Self-oscillating computational models for the vocal folds, driven by the pressure predicted from the Bernoulli relation were first developed in the late 1960s by Flanagan [6]. These basic models for the vocal folds comprise one or two masses coupled to a spring forming an oscillating mass-spring system. These simple but elegant models successfully captured the self-sustained vibration of the vocal folds. Multi-mass models were subsequently developed by Titze in the mid-1970s [29] and similar models were used with variations until the mid-1990s when a body-cover model for the two-mass model was developed by Story and Titze [27] to incorporate the multi-layered nature of the vocal folds. Even though the early lumped mass models were elegant in concept, there is considerable doubt whether they represent the actual geometry and viscoelastic properties of the vocal folds adequately enough to identify voice disorders and special voice qualities [1].

In the mid-1990s, more elaborate models for the vocal folds were developed based on continuum models. A finite element method was used by Alipour and Titze [3] to model the vocal fold deformation, coupled to the flow field obtained through a Navier–Stokes solver. Finite element methods proved much higher accuracy and predictive power than lumped multi-mass models, and were also more suited for handling complex geometries and driving forces. More elaborate models were developed [1, 2], accounting for the transverse isotropy and layered structure of

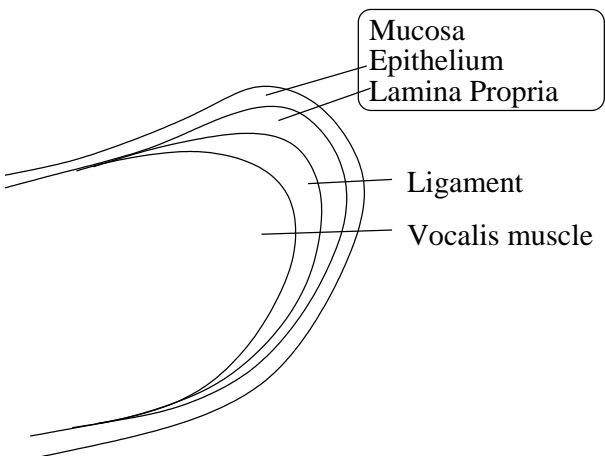


Figure 2: Sketch of the layered structure of the vocal fold. The mucosa (cover) consists of the epithelium and the lamina propria. The ligament is between the cover and the vocalis muscle.

the vocal folds, still assuming small deformations. In 2003, the presence of the false vocal folds was investigated in [23] using a finite element model. Recently, a sharp-interface immersed-boundary method was developed in [15] to simulate the fluid-structure interaction between an incompressible fluid flow and vocal folds with a linear viscoelastic model.

Recently, numerical simulations of phonation based on the compressible Navier–Stokes equations have been performed [33, 34, 32]. Like in direct numerical simulation, high order discretization methods have been preferred for the numerical solution of the compressible Navier–Stokes equations in aeroacoustics, because higher order methods are more efficient for high accuracy requirements than low order methods.

In this paper, we employ a high order finite difference approach based on summation by parts (SBP) operators [28, 9, 8] to solve the compressible Navier–Stokes equations. The compressible Navier–Stokes equations have been chosen to simulate not only the dynamics of the fluid motion but also the generation and propagation of sound waves [31]. A high-order method was chosen because of high accuracy requirements in fluid simulation of sound generation [31]. Opposed to conventional difference approximations, our high order finite difference methods have the advantage of being constructed to be strictly stable for linear hyperbolic and parabolic problems even for non-periodic boundary conditions. The sixth order SBP operator [28], which is third order accurate near the boundaries, is employed to discretize the first derivatives in the 2D compressible Navier–Stokes equations. The second derivatives in the compressible Navier–Stokes equations and the elastodynamic equations are approximated by applying the SBP operator for the first derivatives twice. The SBP operator has previously been used to simulate aeolian tones [19]. The Navier–Stokes equations in conservative form are expressed in perturbation form [25, 18, 19] to minimize rounding errors caused by cancellation in low Mach number flow computations.

Utilizing similar high order finite difference methods, we have also developed an explicit solver for the Lagrangean field equations of structural mechanics and coupled it to our solver for the compressible Navier–Stokes equations in an ALE formulation. Since during phonation, the vocal folds undergo large displacements from their equilibrium configuration, a finite-strain model is needed to model the structure accurately. Our implementation for the structure solver can solve for the dynamic response of the structure due to external loads such as the traction force from a fluid flow. It differs from typical finite-element implementations, in particular with regard to the traction boundary condition which is not trivial to impose in a strong formulation. This issue is elaborated upon below. The advantage of this approach over unstructured methods is that we can have structured grids in both domains (fluid and structure) and matching grid points on the interface without need for interpolation, which increases the accuracy of the computation. Finite element and Cartesian grid immersed-boundary methods have the advantage over structured finite difference methods of handling complex domains better. In this study, we only consider simple domains in 2D. P. Šidlof [26] notes that the vortex dynamics in 2D and 3D are substantially different and that only the 3D simulation can yield reliable results. Nevertheless, 2D numerical methods are prerequisites for the development of 3D ones.

This paper is organized as follows: We start by describing finite strain theory of structural mechanics and continue to present the Navier–Stokes equations of fluid dynamics in perturbation formulation. Then the explicit fluid-structure coupling scheme is outlined. In the next chapter, we present the high order finite difference method and the explicit Runge–Kutta time integration scheme. Results and conclusions are stated at the end.

Finite strain theory

Notation

Finite strain theory is well developed, but the different notations found in the literature can be confusing and sometimes misleading. Therefore, a thorough explanation of basic quantities is warranted here. Let a deformable body occupy some region Ω_0 in space (cf. figure 3). With every particle in the body a coordinate vector $\mathbf{X} = (X, Y, Z)$ called the reference coordinate of the particle is associated. The set Ω_0 is called the reference configuration of the body. As the body translates, rotates and deforms through space, the particle originally at position \mathbf{X} is now at a new position $\mathbf{x} = (x, y, z)$ in the current configuration of the body Ω . A mapping can be defined that associates each reference coordinate with the current coordinate, $\mathbf{x} = \tilde{\phi}(\mathbf{X}, t)$. The displacement from the reference configuration is then $\phi(\mathbf{X}, t) = \tilde{\phi}(\mathbf{X}, t) - \mathbf{X}$. A small line element in the reference configuration $d\mathbf{X}$ transforms to $dx_i = (\partial x_i / \partial X_\alpha) dX_\alpha = F_{i\alpha} dX_\alpha$, where $\mathbf{F} = \nabla_{\mathbf{X}} \tilde{\phi}(\mathbf{X}, t)$ is the deformation gradient. For later convenience, also define $\mathbf{B} = \mathbf{F}^{-T}$ so that $B_{i\alpha} = \partial X_\alpha / \partial x_i$. Tensor notation provides a compact way to write the equations. Here, use will be made of both tensor and index notation.

Governing equations

Neglecting external forces, the Lagrangean field equations [20] which describe the motion of the body, expressed in terms of the nominal stress tensor \mathbf{S} are

$$\frac{\partial S_{\alpha i}}{\partial X_\alpha} = \rho_0 \ddot{\phi}_i. \quad (1)$$

Here, ρ_0 is the density of the body in the reference configuration. Superscript dots denote Lagrangean time derivatives at fixed \mathbf{X} , also known as material time derivatives, i.e.

$$\dot{\phi} \equiv \left. \frac{\partial \phi(\mathbf{X}, t)}{\partial t} \right|_{\mathbf{X}} \equiv \frac{\partial \phi}{\partial t}.$$

Constitutive relations

Define the right Cauchy–Green deformation tensor as $\mathbf{C} = \mathbf{F}^T \mathbf{F}$ and the Green strain tensor $\mathbf{E} = \frac{1}{2}(\mathbf{C} - \mathbf{1})$ where $\mathbf{1}$ is the identity tensor. It is often convenient to consider the elastic properties of a homogeneous material to be derived from a strain energy function $W(\mathbf{E})$ depending on the Green strain tensor only. Such a material is called hyperelastic and this assumption is frequently used in modeling of biological tissues. With this functional dependence, objectivity is asserted [21], i.e. the stored elastic energy is unaffected by superimposed rigid translations and rotations. When there is no deformation, i.e. $\mathbf{F} = \mathbf{1}$ and $\mathbf{E} = \mathbf{0}$ the strain energy must reduce to zero, so that $W(\mathbf{0}) = 0$. The second Piola–Kirchhoff stress tensor (2PK for short) in hyperelasticity is

$$\Sigma = \frac{\partial W(\mathbf{E})}{\partial \mathbf{E}} = 2 \frac{\partial W(\mathbf{C})}{\partial \mathbf{C}} \quad (2)$$

where the partial derivative is to be interpreted as $\Sigma_{ij} = \partial W / \partial E_{ij}$. The nominal stress is in turn obtained by $\mathbf{S} = \Sigma \mathbf{F}^T$. The constitutive model for the material is in the functional form of W

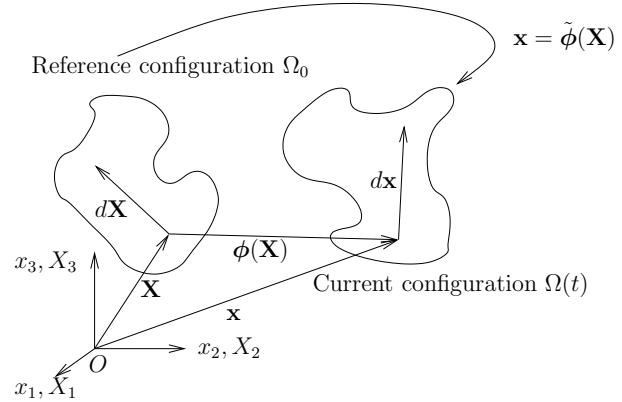


Figure 3: Variables in continuum deformation

which can be an explicit expression for the components of \mathbf{E} (strain-based formulation), but it is often easier to define a material model in terms of the principal invariants of the Cauchy-Green tensor \mathbf{C} (invariant-based formulation), namely $W = W(\mathbf{C}) = W(I_1(\mathbf{C}), I_2(\mathbf{C}), I_3(\mathbf{C}))$ where

$$I_1(\mathbf{C}) = \text{tr}(\mathbf{C}), \quad I_2(\mathbf{C}) = \frac{1}{2}(I_1(\mathbf{C})^2 - \text{tr}(\mathbf{C}^2)) \quad \text{and} \quad I_3(\mathbf{C}) = \det \mathbf{C}.$$

In the invariant-based framework, the derivatives of the invariants with respect to the symmetric deformation tensor are

$$\frac{\partial I_1(\mathbf{C})}{\partial \mathbf{C}} = \mathbf{1}, \quad \frac{\partial I_2(\mathbf{C})}{\partial \mathbf{C}} = \text{tr}(\mathbf{C})\mathbf{1} - \mathbf{C} \quad \text{and} \quad \frac{\partial I_3(\mathbf{C})}{\partial \mathbf{C}} = \mathbf{C}^{-1} \det \mathbf{C}. \quad (3)$$

The recipe for obtaining the nominal stress in the body for a given deformation \mathbf{F} is then $\mathbf{F} \rightarrow \mathbf{C} \rightarrow I_{1,2,3}/\mathbf{E} \rightarrow W \rightarrow \Sigma \rightarrow \mathbf{S}$.

Invariant-based formulations

Consider the neo-Hookean type strain energy function given as $W(\mathbf{C}) = W(I_1(\mathbf{C}), I_3(\mathbf{C})) = \frac{\mu}{2}(I_1 - 3) - \frac{\mu}{2} \ln I_3 + \frac{\lambda}{8}(\ln I_3)^2$. To obtain The 2PK stress for this model, use the definition (2) and the invariant derivatives (3) to obtain

$$\Sigma = 2 \frac{\partial W}{\partial \mathbf{C}} = 2 \frac{\partial W}{\partial I_1} \frac{\partial I_1}{\partial \mathbf{C}} + 2 \frac{\partial W}{\partial I_3} \frac{\partial I_3}{\partial \mathbf{C}} = \mu \mathbf{1} + \left(\frac{\lambda}{2} \ln \det \mathbf{C} - \mu \right) \mathbf{C}^{-1}. \quad (4)$$

For a rigid body motion, the deformation gradient is a an orthogonal tensor which implies that \mathbf{C} is the identity tensor. So, for this model, $\Sigma(\mathbf{C} = \mathbf{1}) = \mathbf{0}$ and $W(\mathbf{C} = \mathbf{1}) = 0$, as expected.

Boundary conditions

(i) Displacement boundary condition

On a boundary Γ_1 where the body is fixed in space, the boundary condition is given directly for the unknown displacements $\phi(\mathbf{X}, t) = \mathbf{f}(\mathbf{X})$, a given function of space. A commonly used boundary condition is that the body should be fixed to its reference configuration on a part of the boundary, in which case one would have $\mathbf{f}(\mathbf{X}) = \mathbf{0}$.

(ii) Condition of traction

If the body experiences traction on a boundary Γ_2 (typically from a surrounding material, e.g. a fluid), a traction condition must be specified on that boundary. In general, this condition can be expressed as $\mathbf{S}^T \mathbf{N} = \mathbf{T}$ where \mathbf{S} is the nominal stress, \mathbf{N} the outward unit normal and \mathbf{T} a given force per unit area on the boundary in the reference configuration.

As an example, consider the case of a static fluid pressure acting on the body. Naturally, the fluid around the body does not recognize anything else than the current configuration Ω of the body, which has some unit outward normal \mathbf{n} . The force \mathbf{t} exerted by the fluid on a small area element da on the boundary of the body is then $\mathbf{t} = -p \mathbf{n} da$, where p is the static fluid pressure. According to Nanson's formula [20], the directed area element $\mathbf{n} da$ in Ω is related to a corresponding element $\mathbf{N} da$ in Ω_0 through $\mathbf{n} da = \det(\mathbf{F}) \mathbf{B} \mathbf{N} da$ with $\mathbf{B} = \mathbf{F}^{-T}$. Thus, the force per unit area in the reference configuration can be written as $\mathbf{T} = \mathbf{t}/da = -p \det(\mathbf{F}) \mathbf{B} \mathbf{N}$. Extension from static pressure to shear stress from a viscous fluid flow is now straightforward. A fluid with stress tensor $\boldsymbol{\sigma}^f$ exerts a force $\mathbf{t} = \boldsymbol{\sigma}^f \mathbf{n} da$ on an area element da . Using Nanson's formula again, the force per unit area in the reference configuration can be written

$$\mathbf{T} = \det(\mathbf{F})\boldsymbol{\sigma}^f \mathbf{B} \mathbf{N}. \quad (5)$$

This formula also includes the static fluid pressure case, for which $\boldsymbol{\sigma}^f = -p\mathbf{1}$. Furthermore, in a compressible viscous fluid, the stress is

$$\boldsymbol{\sigma}^f = \left(-p - \frac{2}{3}\mu^f \nabla \cdot \mathbf{u}^f \right) \mathbf{1} + \mu^f \left(\nabla \mathbf{u}^f + (\nabla \mathbf{u}^f)^T \right) \quad (6)$$

where μ^f is the fluid viscosity and \mathbf{u}^f is the fluid velocity.

Transformation

In order to transform the reference configuration to a computational domain, a set of computational coordinates ξ, η is introduced. The coordinates in the reference configuration can then be written $X = X(\xi, \eta), Y = Y(\xi, \eta)$. Since the transformation is invertible, the opposite relations $\xi = \xi(X, Y), \eta = \eta(X, Y)$ hold as well. Differentiating these transformations yields two vector equations for the Jacobian matrices where one must be the inverse of the other, hence the metric identities are $J^{-1}\xi_X = Y_\eta, J^{-1}\xi_Y = -X_\eta, J^{-1}\eta_X = -Y_\xi, J^{-1}\eta_Y = X_\xi$ where

$$J^{-1} = X_\xi Y_\eta - X_\eta Y_\xi \quad (7)$$

is the Jacobian determinant of the transformation. Transforming the Lagrangean field equations to computational coordinates gives

$$J^{-1}\rho_0 \ddot{\phi} = (J^{-1}\xi_X \mathbf{S}_1 + J^{-1}\xi_Y \mathbf{S}_2)_\xi + (J^{-1}\eta_X \mathbf{S}_1 + J^{-1}\eta_Y \mathbf{S}_2)_\eta - \mathbf{S}_1[(J^{-1}\xi_X)_\xi + (J^{-1}\eta_X)_\eta] - \mathbf{S}_2[(J^{-1}\xi_Y)_\xi + (J^{-1}\eta_Y)_\eta], \quad (8)$$

where the notation $S_{\alpha i} = (\mathbf{S}_\alpha)_i$ has been used, i.e. \mathbf{S}_1 and \mathbf{S}_2 viewed as column vectors are the columns of \mathbf{S}^T . The terms in square brackets cancel because of the metric identities and the fact that the partial derivatives commute. What remains is

$$\ddot{\phi} = \frac{1}{J^{-1}\rho_0} \left[(\widehat{\mathbf{S}}_1)_\xi + (\widehat{\mathbf{S}}_2)_\eta \right] \quad (9)$$

where $\widehat{\mathbf{S}}_1 = J^{-1}\mathbf{S}^T \nabla \xi$ and $\widehat{\mathbf{S}}_2 = J^{-1}\mathbf{S}^T \nabla \eta$ are transformed momentum flux vectors. Finally, the transformed equations of motion (9) are rewritten as a system of equations with only first time derivatives. Defining $\psi = \dot{\phi}$, the system becomes

$$\begin{cases} \dot{\psi} = \frac{1}{J^{-1}\rho_0} \left[(\widehat{\mathbf{S}}_1)_\xi + (\widehat{\mathbf{S}}_2)_\eta \right] \\ \dot{\phi} = \psi \end{cases} \quad (10)$$

where the unknowns are the displacements ϕ and the velocities ψ . This system has 4 unknowns in 2D.

Compressible Navier–Stokes equations

The perturbation formulation is used to minimize cancellation errors when discretizing the Navier–Stokes equations for compressible low Mach number flow [25, 18]. The 2D compressible Navier–Stokes equations in conservative form can be expressed in perturbation form as [19, 14]

$$\mathbf{U}'_t + \mathbf{F}'_x + \mathbf{G}'_y = \mathbf{F}^v_x + \mathbf{G}^v_y, \quad (11)$$

where the vector \mathbf{U}' denotes the perturbation of the conservative variables with respect to the stagnation values. \mathbf{U}' and the inviscid (superscript c) and viscous (superscript v) flux vectors are defined by

$$\mathbf{U}' = \begin{pmatrix} \rho' \\ (\rho u)' \\ (\rho v)' \\ (\rho E)' \end{pmatrix}, \quad \mathbf{F}^{c'} = \begin{pmatrix} (\rho u)' \\ (\rho u)' u' + p' \\ (\rho v)' u' \\ (\rho_0 H_0 + (\rho H)') u' \end{pmatrix}, \quad \mathbf{G}^{c'} = \begin{pmatrix} (\rho v)' \\ (\rho u)' v' \\ (\rho v)' v' + p' \\ (\rho_0 H_0 + (\rho H)') v' \end{pmatrix},$$

$$\mathbf{F}^{v'} = \begin{pmatrix} 0 \\ \tau'_{xx} \\ \tau'_{xy} \\ \tau'_{xx} u' + \tau'_{xy} v' + \kappa T'_x \end{pmatrix}, \quad \mathbf{G}^{v'} = \begin{pmatrix} 0 \\ \tau'_{yx} \\ \tau'_{yy} \\ \tau'_{yx} u' + \tau'_{yy} v' + \kappa T'_y \end{pmatrix}.$$

The subscripts in (11) subsequently denote derivatives. We assume perfect gas. The perturbation variables (superscript $'$) are defined with respect to their stagnation values (subscript 0), i.e. $\rho' = \rho - \rho_0$, $(\rho \mathbf{u})' = \rho \mathbf{u}$, $(\rho E)' = \rho E - (\rho E)_0$, $(\rho H)' = (\rho E)' + p'$, $\mathbf{u}' = \frac{(\rho \mathbf{u})'}{\rho_0 + \rho'}$, $p' = (\gamma - 1)[(\rho E)' - \frac{1}{2}((\rho \mathbf{u})' \cdot \mathbf{u}')]$, $\tau' = \mu(\nabla \mathbf{u}' + (\nabla \mathbf{u}')^T) - \frac{2}{3}\mu(\nabla \cdot \mathbf{u}')\mathbf{I}$, $T' = \frac{p'/R - \rho' T_0}{\rho_0 + \rho'}$. Time is t , and x and y are the Cartesian coordinates. Denoted by ρ is the density, u and v the x - and y -direction velocities, E the specific total energy, p the pressure, $\gamma = 1.4$ the ratio of specific heats for air, R the specific gas constant, μ viscosity determined from the Sutherland law $\frac{\mu}{\mu_0} = (\frac{T}{T_0})^{1.5} \frac{1+S_c}{\frac{T}{T_0}+S_c}$ with the nondimensional Sutherland constant $S_c = \frac{110}{301.75}$ and κ the heat conduction coefficient determined from the constant Prandtl number $\text{Pr} = 1$. The quantities ρ_0 , $(\rho E)_0$ and $(\rho H)_0$ denote the stagnation quantities of density, total energy density and total enthalpy density, respectively. The viscous flux vectors $\mathbf{F}^{v'}$ and $\mathbf{G}^{v'}$ are the same as for the standard conservative form, except for using the temperature perturbation T' instead of temperature T for the heat flux terms. The momentum density and velocity perturbations are taken as the same as their unperturbed counterparts, i.e. $(\rho \mathbf{u})' = \rho \mathbf{u}$ and $\mathbf{u}' = \mathbf{u}$, cf. the definition of \mathbf{U}' with respect to $\mathbf{U}_0 = (\rho_0, 0, 0, (\rho E)_0)^T$ above. The 2D conservative compressible Navier–Stokes equations in perturbation form (11) are written in dimensional form, while their nondimensional form with ρ_0 , stagnation speed of sound c_0 , and $\rho_0 c_0^2$ as reference values of density, velocity, and pressure, respectively, has actually been used in the computations.

General moving geometries are treated by a time dependent coordinate transformation $\tau = t$, $\xi = \xi(t, x, y)$, $\eta = \eta(t, x, y)$. The transformed 2D conservative compressible Navier–Stokes equations in perturbation form read

$$\hat{\mathbf{U}}'_\tau + \hat{\mathbf{F}}'_\xi + \hat{\mathbf{G}}'_\eta = 0, \quad (12)$$

where $\hat{\mathbf{U}}' = J^{-1} \mathbf{U}'$, $\hat{\mathbf{F}}' = J^{-1}(\xi_\tau \mathbf{U}' + \xi_x(\mathbf{F}^{c'} - \mathbf{F}^{v'}) + \xi_y(\mathbf{G}^{c'} - \mathbf{G}^{v'}))$ and $\hat{\mathbf{G}}' = J^{-1}(\xi_\tau \mathbf{U}' + \eta_x(\mathbf{F}^{c'} - \mathbf{F}^{v'}) + \eta_y(\mathbf{G}^{c'} - \mathbf{G}^{v'}))$. The x - and y -derivatives in the viscous flux vectors $\mathbf{F}^{v'}$ and $\mathbf{G}^{v'}$ are expressed using the chain rule, e.g. $u'_x = u'_\xi \xi_x + u'_\eta \eta_x$ and $u'_y = u'_\xi \xi_y + u'_\eta \eta_y$. The Jacobian determinant of the transformation J is determined by $J^{-1} = x_\xi y_\eta - x_\eta y_\xi$, and the metric terms by $J^{-1} \xi_x = y_\eta$, $J^{-1} \xi_y = -x_\eta$, $J^{-1} \eta_x = -y_\xi$, $J^{-1} \eta_y = x_\xi$.

Fluid-structure interaction

ALE formulation for fluid solver

The displacement of the structure interface determines the shape of the fluid domain and the structure velocity at the interface determines the internal grid point velocities in the fluid domain. The right and left boundaries of the fluid domain are the out- and inflow, respectively. The top and bottom parts of the fluid domain are bounded by the flexible vocal folds and the inner wall of the airpipe which is assumed to be rigid. We do not assume symmetry; the motion of the two vocal folds are solved for individually. In our ALE formulation, the positions and velocities of the grid points in the fluid domain are a linear interpolation of the positions and velocities of the structure at the interface. Figure 4 shows the given structure velocity with a bold arrow and the interpolated grid point velocities \dot{x}, \dot{y} (thin arrow) for three grid lines.

To obtain the time derivative of J^{-1} as needed in (12), a geometric invariant [30] is used. This geometric conservation law states that $(J^{-1})_\tau + (J^{-1}\xi_t)_\xi + (J^{-1}\eta_t)_\eta = 0$. The time derivatives of the computational coordinates ξ, η can here be obtained from the grid point velocities \dot{x}, \dot{y} as $\xi_t = -(\dot{x}\xi_x + \dot{y}\xi_y)$, $\eta_t = -(\dot{x}\eta_x + \dot{y}\eta_y)$ which can be seen by differentiating the transformation with respect to τ .

Traction boundary condition in transformed coordinates

The traction boundary condition is somewhat strange, because it does not directly give a relation for the unknowns that must be satisfied, unlike the displacement boundary condition. Rather, as will be shown, it specifies the flux of momentum on the boundary. As can be seen in equation (5), the unit normal is needed for the boundary condition. This can easily be constructed from the coordinate transformation. For example, a coordinate line where $\eta = \text{const}$ is a level curve for the function $\eta(X, Y)$. Hence, the gradient $\nabla_X \eta$ is perpendicular to this line and the unit normal is then simply $\mathbf{N} = \nabla \eta / |\nabla \eta|$ (where the subscript X has been dropped for convenience), pointing in the direction of increasing η . A boundary condition for viscous fluid stress on a boundary where $\eta = \eta_{\max}$ is then obtained by inserting the unit normal into $\mathbf{S}^T \mathbf{N} = \mathbf{T}$, with \mathbf{T} given by eq. (5), hence $\mathbf{S}^T \nabla \eta = \det(\mathbf{F}) \boldsymbol{\sigma}^f \mathbf{B} \nabla \eta$. Since \mathbf{B} is just the inverse of a 2-by-2 matrix, it can be explicitly calculated in terms of the deformation gradient components. Furthermore, multiply both sides by J^{-1} to get the final expression for the momentum flux in the η -direction,

$$\widehat{\mathbf{S}_2} \equiv J^{-1} \mathbf{S}^T \nabla \eta \stackrel{!}{=} J^{-1} \boldsymbol{\sigma}^f \begin{pmatrix} F_{22} & -F_{21} \\ -F_{12} & F_{11} \end{pmatrix} \nabla \eta. \quad (13)$$

This is the boundary condition that must be fulfilled, i.e. when calculating the η -derivative in (9), we use the value (13) at the boundary. A boundary condition for the ξ -direction can be constructed similarly if needed.

Description of fluid-structure interaction algorithm

First, we construct the fixed reference configuration for the structure, set the initial displacements and velocities to zero. The initial fluid domain is then uniquely determined by the reference boundary of the structure. Initially, the fluid grid points have zero velocity and the wall

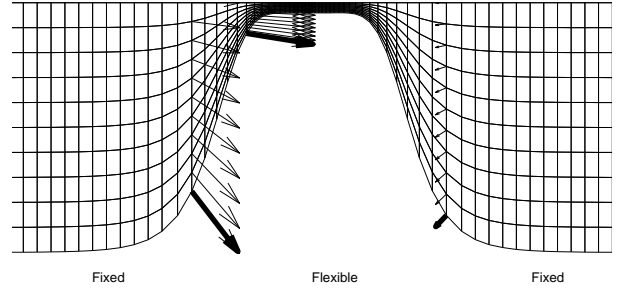


Figure 4: The boundary of the fluid domain consists of fixed and flexible parts. The velocity at the boundary of the flexible part determines the internal grid point velocity. Only half domain shown.

does not move. We then take one time step for the fluid with imposed pressure boundary conditions at the inflow, zero initial conditions for the perturbation variables \mathbf{U}' and adiabatic no-slip conditions, i.e. $\mathbf{u} = 0$ and $\partial T / \partial n = 0$ on the wall. After the first fluid time step, the viscous fluid stress on the wall is calculated based on the new fluid velocities and pressures using (6). These fluid stresses are passed on to the structure via the traction boundary condition (13). With this boundary condition imposed, one time step is taken for the structure. The solution for the structure gives the velocity and displacement on the boundary (and all internal points) and these are then used to generate the new fluid mesh and internal grid point velocities. This procedure is then repeated for as many time steps as required.

High order finite difference method

Summation by parts operators

Let $v_j, j = 0, \dots, N$, be an approximation to the exact solution $u(x_j)$ at the grid point $x_j = jh$ where $h = 1/N$. The discrete scalar product and norm are [28] $(u, v)_h = hu^T Hv$, $\|u\|_h^2 = (u, u)_h$ where the norm matrix H is diagonal and positive definite. The *summation by parts* (SBP) property, analogous to integration by parts in the continuous case, is satisfied, if $(u, Qv)_h = u_N v_N - u_0 v_0 - (Qu, v)_h$ for a difference operator Q . Let the operator Q be defined in terms of B as $hQ = H^{-1}B$. The SBP property can be rewritten as $hu^T HQv = u^T \text{diag}(-1, 0, \dots, 0, 1)v - h(Qu)^T Hv$ and rearranged to $hu^T (HQ + Q^T H)v = u^T \text{diag}(-1, 0, \dots, 0, 1)v$. Now, H is diagonal by definition so $H = H^T$, hence $u^T (HhQ + (HhQ)^T)v = u^T \text{diag}(-1, 0, \dots, 0, 1)v$. Using the definition of Q and the fact that u and v are arbitrary, we get $B + B^T = \text{diag}(-1, 0, \dots, 0, 1)$.

The difference operator Q is an approximation to the first derivative, i.e. $(Qv)_j \approx \frac{du(x_j)}{dx}$. If Q is accurate of order 2τ in the interior, then there is a diagonal norm matrix H , such that Q is accurate of order τ near the boundaries [28]. When $\tau = 3$ which is the case considered here, there is a one-parameter family of operators Q . One of the elements in the matrix of Q can be set to zero in such a way that the bandwidth of the matrix is minimized to obtain a unique matrix Q which yields a 6th order accurate operator in the interior. Thus, the global order of accuracy of the present SBP operator Q is $\tau + 1 = 4$ [9, 8].

Second derivatives are approximated by applying the SBP operator Q twice. Alternative discretizations of second derivatives [16, 11] are discussed in [19]. Opposed to conventional difference operators, SBP operators allow energy estimates for the discrete problems similar to the ones for the continuous problems, which are approximated. Thus, SBP operators yield strictly stable schemes for general boundary conditions.

If the x -derivative in the convection diffusion equation $u_t + au_x = bu_{xx}$, where a and b are assumed to be constant and $b > 0$, is approximated by a standard central p th order finite difference operator $Q_x^{(p)}$ and the time derivative by an explicit Runge-Kutta method, the von Neumann stability analysis leads to the stability condition $\Delta t(-a\hat{Q}^{(p)} + b(\hat{Q}^{(p)})^2) \in S$, where $\hat{Q}^{(p)}$ is the Fourier transform of $Q_x^{(p)}$ and S the stability domain of the Runge–Kutta method. $\hat{Q}^{(p)} \frac{\Delta x}{i}$ is the approximate wave number $\tilde{k}\Delta x$. For SBP operators, the stability condition is more restrictive, because $\Delta t \| -aQ_x^{(p)} + b(Q_x^{(p)})^2 \| \leq R < R_1$ is required, where the open semicircle $\{z \in \mathbb{C} \mid |z| < R_1 \text{ and } \text{Real}(z) < 0\}$ is contained in the stability domain S [12]. In practical computations, however, it has been possible to use von Neumann stability condition with a safety margin. The von Neumann stability condition for the standard central sixth order difference operator $Q_x^{(6)}$ and the classical fourth order explicit Runge-Kutta method reads $CFL = \frac{|a|\Delta t}{\Delta x} \leq 1.783$ for $b = 0$ and $VNN = \frac{|b|\Delta t}{\Delta x^2} \leq 1.124$ for $a = 0$, while $CFL \leq 2.828$ for

$b = 0$ and $VNN \leq 2.828$ for $a = 0$ is required for the standard central second order operator $Q_x^{(2)}$. Note that $(Q_x^{(6)}\mathbf{u})_j = \frac{1}{\Delta x}(\frac{1}{60}u_{j+3} - \frac{3}{20}u_{j+2} + \frac{3}{4}u_{j+1} - \frac{3}{4}u_{j-1} + \frac{3}{20}u_{j-2} - \frac{1}{60}u_{j-3})$ and $\hat{Q}^{(6)} = \frac{i}{\Delta x}[\frac{3}{2}\sin(k\Delta x) - \frac{3}{10}\sin(2k\Delta x) + \frac{1}{30}\sin(3k\Delta x)]$, where k is the wave number in this subsection. With this information, the stability condition of a second order central method for the compressible Navier–Stokes equations in [17] can be easily generalized for the present high order method.

Approach for compressible Navier–Stokes equations

The transformed 2D compressible Navier–Stokes equations in perturbation form (12) are solved on a rectangle, where $\xi = 1$ and $\xi = jmax$ represent the inlet and outlet boundaries of the vocal tract, respectively, and $\eta = 1$ and $\eta = kmax$ correspond to the lower and upper walls of the vocal tract, respectively. The ξ - and η -derivatives in the metric terms are discretized by Strand’s 3-6 SBP operator [28]. The viscous flux vectors are discretized by approximating the first ξ and η derivatives of u' , v' and T' , by Strand’s 3-6 SBP operator. After the flux vectors $\hat{\mathbf{F}}'$ and $\hat{\mathbf{G}}'$ are computed at all grid points, $\hat{\mathbf{F}}'_\xi$ and $\hat{\mathbf{G}}'_\eta$ are approximated by employing Strand’s 3-6 SBP operator once more. The classical fourth order explicit Runge-Kutta method is used for time integration (see below). Spurious high wave number oscillations are suppressed by a sixth order explicit filter [19].

Boundary conditions

No-slip adiabatic wall boundary conditions and the Navier–Stokes Characteristic Boundary Conditions (NSCBC) technique by Poinsot and Lele in [22] are employed.

At the inflow, pressure, temperature and velocity in the y -direction are imposed as $p = p_{atm} + \Delta p$, $T = T_0 = 310$ K, and $v = 0$, respectively. The x -velocity u at the inflow and the pressure p at the solid walls are taken from the Navier–Stokes solution at those boundaries. At the outflow, the amplitudes of the characteristic waves $\mathcal{L}_1 = \lambda_1(p_x - \rho c u_x)$, $\mathcal{L}_2 = \lambda_2(c^2 \rho_x - p_x)$, $\mathcal{L}_3 = \lambda_3 v_x$, $\mathcal{L}_4 = \lambda_4(p_x + \rho c u_x)$ are set to zero for ingoing waves. Imposing the atmospheric pressure p_{atm} at the outlet would lead to a well-posed problem but at the cost of numerical reflections. To keep numerical reflections low and the pressure close to atmospheric pressure, the amplitude of the ingoing wave is set to $\mathcal{L}_1 = K(p - p_{atm})$ where the constant K , proposed by Rudy and Strikwerda [24] is taken as $K = \sigma(1 - M^2)c/L$. Here, σ is a constant, M is the maximum Mach number, c the speed of sound and L a characteristic size of the domain. The choice $\sigma = 0$ corresponds to a perfectly non-reflecting case but without information about the atmospheric pressure. The value 0.25 was used in this study [22]. For reverse flow (i.e. negative x -velocity) at the outlet, we set $\mathcal{L}_1 = \mathcal{L}_2 = \mathcal{L}_3 = 0$.

Approach for the Langrangean field equations

The transformed 2D Lagrangean field equations (10) are discretized in the same way as the Navier–Stokes equations. The deformation gradient \mathbf{F} and the derivatives of the flux vectors are approximated at all grid points using Strand’s 3-6 SBP operator alike.

The computation of the right-hand side (9) for an internal grid point (i, j) is detailed below. At and near boundaries, the corresponding coefficients of the SBP operator $Q^{(6)}$ are used.

- Given the displacement field $\phi = (\phi^1, \phi^2)^T$, calculate the derivative with respect to the computational coordinate ξ using the high-order finite difference scheme $Q = Q^{(6)}$

$$\left(\frac{\partial \phi^k}{\partial \xi} \right)_{i,j} \approx Q_\xi \phi_{i,j}^k = -\frac{1}{60} \phi_{i-3,j}^k + \frac{3}{20} \phi_{i-2,j}^k - \frac{3}{4} \phi_{i-1,j}^k + \frac{3}{4} \phi_{i+1,j}^k - \frac{3}{20} \phi_{i+2,j}^k + \frac{1}{60} \phi_{i+3,j}^k$$

for both components k of the displacement. Approximate the η derivative similarly. The components of the deformation gradient at point (i, j)

$$(F_{k\alpha})_{i,j} = \left(\frac{\partial x_k}{\partial X_\alpha} \right)_{i,j} = \delta_{k\alpha} + \left(\frac{\partial \phi^k}{\partial X_\alpha} \right)_{i,j} = \delta_{k\alpha} + \left(\frac{\partial \phi^k}{\partial \xi} \right)_{i,j} \left(\frac{\partial \xi}{\partial X_\alpha} \right)_{i,j} + \left(\frac{\partial \phi^k}{\partial \eta} \right)_{i,j} \left(\frac{\partial \eta}{\partial X_\alpha} \right)_{i,j}.$$

are then approximated by using the approximation of $(\partial \phi^k / \partial \xi)_{i,j}$ etc. above and by also discretizing the metric terms $(\partial \xi / \partial X_\alpha)_{i,j}$ etc. by the 6th order SBP operator.

2. Evaluate the components of the right Cauchy–Green deformation tensor according to $(C_{\alpha\beta})_{i,j} = (F_{k\alpha})_{i,j} (F_{k\beta})_{i,j}$.
3. Form the necessary functions of \mathbf{C} as required by the material model, e.g. $(\det(\mathbf{C}))_{i,j} = (C_{11})_{i,j} (C_{22})_{i,j} - (C_{12})_{i,j} (C_{21})_{i,j}$.
4. Calculate the components of the 2PK stress using the material model, e.g. $(\Sigma_{\alpha\beta})_{i,j} = \mu_{i,j} \delta_{\alpha\beta} + (\lambda_{i,j} \ln(\det \mathbf{C})_{i,j} / 2 - \mu_{i,j}) (\mathbf{C}^{-1})_{\alpha\beta}$ where the space-dependent Lamé parameters λ and μ are evaluated at grid point (i, j) , i.e. $\lambda_{i,j} = \lambda(\mathbf{X}_{i,j})$.
5. Evaluate the components of the nominal stress as $(S_{\alpha k})_{i,j} = (\Sigma_{\alpha\beta})_{i,j} (F_{k\beta})_{i,j}$.
6. Determine the momentum fluxes in the ξ and η directions,

$$\begin{aligned} \widehat{(\mathbf{S}_1)}_{i,j} &= (J^{-1})_{i,j} \begin{bmatrix} (S_{11})_{i,j} (\partial \xi / \partial X)_{i,j} + (S_{21})_{i,j} (\partial \xi / \partial Y)_{i,j} \\ (S_{12})_{i,j} (\partial \xi / \partial X)_{i,j} + (S_{22})_{i,j} (\partial \xi / \partial Y)_{i,j} \end{bmatrix}, \\ \widehat{(\mathbf{S}_2)}_{i,j} &= (J^{-1})_{i,j} \begin{bmatrix} (S_{11})_{i,j} (\partial \eta / \partial X)_{i,j} + (S_{21})_{i,j} (\partial \eta / \partial Y)_{i,j} \\ (S_{12})_{i,j} (\partial \eta / \partial X)_{i,j} + (S_{22})_{i,j} (\partial \eta / \partial Y)_{i,j} \end{bmatrix}, \end{aligned}$$

where again we use the discrete metric terms. The discrete Jacobian $(J^{-1})_{i,j}$ is calculated from the discrete metric terms as shown earlier in (7).

7. The derivatives of the flux vectors with respect to the computational coordinates are obtained with the 6th order central scheme, e.g. for the ξ -derivative,

$$\begin{aligned} \left(\frac{\partial \widehat{(\mathbf{S}_1)}}{\partial \xi} \right)_{i,j} &\approx (Q_\xi \widehat{(\mathbf{S}_1)})_{i,j} = -\frac{1}{60} (\widehat{(\mathbf{S}_1)})_{i-3,j} + \frac{3}{20} (\widehat{(\mathbf{S}_1)})_{i-2,j} - \frac{3}{4} (\widehat{(\mathbf{S}_1)})_{i-1,j} + \\ &\quad \frac{3}{4} (\widehat{(\mathbf{S}_1)})_{i+1,j} - \frac{3}{20} (\widehat{(\mathbf{S}_1)})_{i+2,j} + \frac{1}{60} (\widehat{(\mathbf{S}_1)})_{i+3,j}. \end{aligned}$$

8. The right hand side of the momentum equation is calculated as

$$\dot{\psi}_{i,j} = \frac{1}{(J^{-1})_{i,j} \rho_0} \left[(Q_\xi \widehat{(\mathbf{S}_1)})_{i,j} + (Q_\eta \widehat{(\mathbf{S}_2)})_{i,j} \right].$$

Time integration

Both the Navier–Stokes (12) and the Lagrangean field equations (10) can be written in the form $\dot{\Phi}^i = \mathbf{f}^i(t, \Phi^i)$ with $\Phi^s = (\phi, \psi)$ and $\Phi^f = \hat{\mathbf{U}}'$, where $i = s$ and $i = f$ stand for structure and fluid, respectively. The semi-discrete equations can be formulated as a 4th order explicit Runge–Kutta scheme for both fields with a time step Δt as

$$\begin{aligned}\mathbf{k}_1 &= \mathbf{f}^i(t_n, \Phi^{i,n}) \\ \mathbf{k}_2 &= \mathbf{f}^i\left(t_n + \frac{\Delta t}{2}, \Phi^{i,n} + \frac{\Delta t}{2}\mathbf{k}_1\right) \\ \mathbf{k}_3 &= \mathbf{f}^i\left(t_n + \frac{\Delta t}{2}, \Phi^{i,n} + \frac{\Delta t}{2}\mathbf{k}_2\right) \\ \mathbf{k}_4 &= \mathbf{f}^i(t_n + \Delta t, \Phi^{i,n} + \Delta t\mathbf{k}_3) \\ \Phi^{i,n+1} &= \Phi^{i,n} + \frac{\Delta t}{6}(\mathbf{k}_1 + 2\mathbf{k}_2 + 2\mathbf{k}_3 + \mathbf{k}_4)\end{aligned}$$

where $\Phi^{i,n}$ is the solution at the old time level n for field i .

Verification of structure method

Method of manufactured solution

An analytical test case for time-dependent problems in hyperelasticity is hard to find. Thus, for verification of the implemented techniques, the method of manufactured solution is used. The idea of the method is to construct a solution somewhat arbitrarily and insert it into the equations to be solved, without any boundary conditions. Since the constructed solution does not, in general, satisfy the equations, one ends up with a nonzero source term. If this source term is included in the original equations, the constructed solution must satisfy the original equation with the source term. To see how this works, rewrite the field equations (1) as

$$\ddot{\phi} - \text{Div}(\mathbf{S}(\phi))/\rho_0 = 0 \quad (14)$$

where Div is the divergence in reference coordinates. Now construct explicitly an arbitrary solution $\varphi(\mathbf{X}, t)$ and insert it into the left hand side of (14) to obtain $\ddot{\varphi} - \text{Div}(\mathbf{S}(\varphi(\mathbf{X}, t))) = \mathbf{R}(\mathbf{X}, t)$ where \mathbf{R} is a residual source term. Thus, φ satisfies the PDE

$$\ddot{\varphi} - \text{Div}(\mathbf{S}(\varphi))/\rho_0 = \mathbf{R}(\mathbf{X}, t). \quad (15)$$

The source term \mathbf{R} can be evaluated analytically for a given deformation φ by means of a symbolic mathematical tool such as Maple.

Test cases

The manufactured solution can be chosen in many different ways, but on physical grounds, it is reasonable to require that $\det \mathbf{F} > 0$ so that the physical domain (current configuration) does not overlap itself. Keeping this requirement in mind, the following test case is considered:

The reference configuration \mathbf{X} is a square occupying the region $-1 \leq X, Y \leq 1$. The deformation is chosen such that the square changes size according to $\varphi(\mathbf{X}, t) = \frac{\mathbf{X}}{2} \sin \omega t$, i.e. at $\omega t = \pi/2$, the square has increased its size to $-3/2 \leq x, y \leq 3/2$ where $(x, y) = (X, Y) + \varphi$. The neo-Hookean material (4) model is used.

Error analysis

Define the error in the discrete solution $\phi_{i,j}$, at a certain time level, as the l_2 norm of the error

$$e = \left[\sum_{i,j} \Delta A_{i,j} |\phi_{i,j} - \varphi_{i,j}|^2 \right]^{1/2}$$

where $\varphi_{i,j} = \varphi(\mathbf{X}_{i,j}, t)$ is the analytical (constructed) solution evaluated at grid point (i, j) and $\Delta A_{i,j}$ is the cell volume (area) J^{-1} associated with grid point (i, j) in the reference configuration.

Verification of time integration

The source term for the test case with given deformation is $\mathbf{R}(\mathbf{X}, t) = -\omega^2 \frac{\mathbf{X}}{2} \sin(\omega t)$. It can be shown that the contribution from the stress tensor vanishes for the neo-Hookean material. The divergence of the stress in the material also vanishes, so the equation being solved is in fact just $\ddot{\phi} = R(\mathbf{X}, t)$. Choosing $\omega = \pi$ and evaluating the solution at $t = 1$ where the analytical solution is $\phi(\mathbf{X}, t = 1) = \varphi(\mathbf{X}, t = 1) = \mathbf{0}$ for different time steps yields the results shown in table 1. The 4th order convergence of the Runge–Kutta scheme is evident. The grid spacing is insignificant here, since each point is decoupled from the others.

Comparison with Abaqus/Explicit

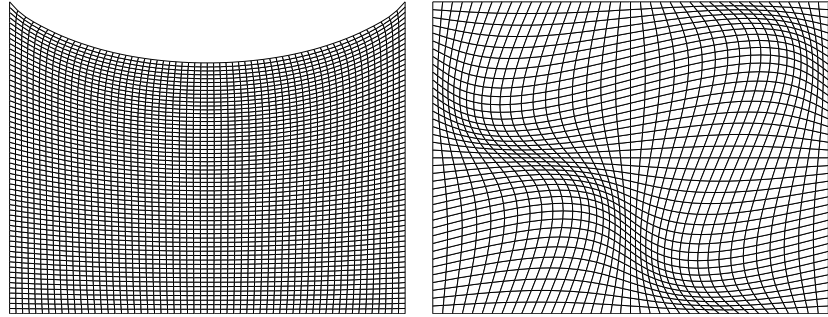
The test case only verified the time integration. To verify the space discretization and the boundary conditions, we consider a square reference domain $-1/2 \leq X, Y \leq 1/2$ for a body where three segments of the boundary are fixed in space and the fourth (top) is subjected to a time-dependent fluid pressure load, see fig. 5(a). When simulating this simple test case, one can ask, for example, what is the y -displacement of the midpoint on the top boundary, as a function of time? This question was investigated using both the previously described finite difference method and Abaqus, a commercial finite-element analysis package developed by Simulia [4].

The material model was the neo-Hookean material (4) with dimensionless Lamé parameters $\mu = 1$, $\lambda = 1$ and density $\rho = 1$. The time-dependent pressure on the top boundary was $P(t) = \sin^2(\pi t/4)$. The input parameters for Abaqus need to be given in the form $C_{10} = \mu/2$ and $D_1 = 2/\kappa$ where $\kappa = (3\lambda + 2\mu)/3$. For the finite-difference simulation, a 121×121 grid was used and a sufficiently small time step so that time integration errors were not dominant. For Abaqus, an unstructured mesh with 3206 linear plane-stress triangular elements was used. The results shown in figure 5(c) indicate a good agreement between the two analyses. The time-dependent behaviour of the displacement is captured well, both in terms of amplitude and phase. This indicates that the traction boundary condition (13) is handled correctly.

Additionally, as a test for the coordinate transformation, a more general domain was considered. For the case of a simple square, the coordinate transformation was $X = \xi - 1/2$, $Y = \eta - 1/2$ where ξ and η are computational coordinates $0 \leq \xi, \eta \leq 1$. Consider now the transformation $X(\xi, \eta) = \xi - 1/2 + d(\xi, \eta)$, $Y(\xi, \eta) = \eta - 1/2 + d(\xi, \eta)$ with $d(\xi, \eta) = 0.08 \sin(2\pi(\xi -$

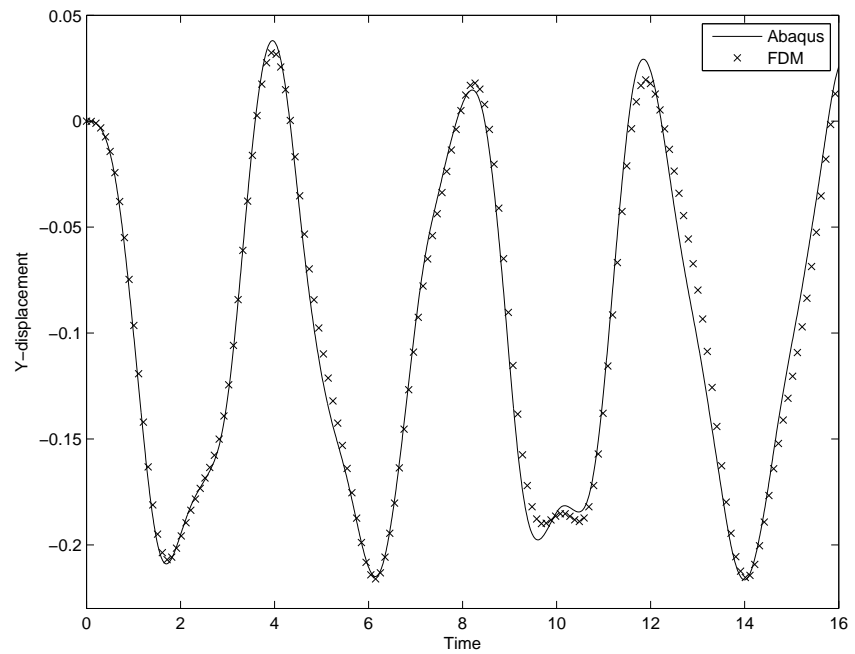
Δt	e	Order
1/32	9.1143×10^{-9}	
1/64	5.6952×10^{-10}	4.0003
1/128	3.5593×10^{-11}	4.0001
1/256	2.2244×10^{-12}	4.0001
1/512	1.3921×10^{-13}	3.9981
1/1024	8.8033×10^{-15}	3.9831
1/2048	6.2144×10^{-16}	3.8244

Table 1: Error as a function of time step for the pulsating square case at time $t = 1$ and $\omega = \pi$.



(a) Geometry for the pressure-loaded square test case. The left, right and bottom boundaries are fixed. The top boundary is loaded with a time-dependent pressure.

(b) Distorted grid.



(c) Comparison of y -displacement of midpoint on top boundary of figure 5(a) in Abaqus/Explicit (—) vs. finite difference method (\times) for a square geometry with pressure load, neo-Hookean material.

Figure 5: Geometry and results for test case

$1/2)) \sin(2\pi(\eta - 1/2))$. The domain is still a square, but the internal grid lines are no longer parallel, as seen in fig. 5(b). Computation on the distorted grid yields the same results as on the Cartesian grid.

Results

Geometry

The initial geometry for the vocal folds is here based on the geometry used in [34] for an oscillating glottis with a given time dependence. The initial shape of the vocal tract including the vocal fold is given as

$$r_w(x) = \frac{D_0 - D_{\min}}{4} \tanh s + \frac{D_0 + D_{\min}}{4}, \quad (16)$$

where r_w is the half height of the vocal tract, $D_0 = 5D_g$ is the height of the channel, $D_g = 4$ mm is the average glottis height, $D_{\min} = 2$ mm is the minimum glottis height, $s = b|x|/D_g - bD_g/|x|$, $c = 0.42$ and $b = 1.4$. For $-2D_g \leq x \leq 2D_g$, the function (16) describes the curved parts of the reference configuration for the top and bottom (with a minus sign) vocal folds.

Vocal fold material parameters

The density in the reference configuration is $\rho_0 = 1043$ kg/m³, corresponding to the measured density of vocal fold tissue as reported by [10]. The Poisson ratio was chosen as $\nu = 0.47$ for the whole tissue, corresponding to a nearly incompressible material with $\nu = 0.5$ being the theoretical incompressible limit. A two-layer model for the vocal folds was used so that the shear modulus varied smoothly¹ from $\mu_c = 3.5$ kPa in the cover to $\mu_l = 4.4$ kPa in the ligament. The Lamé parameter λ , as a function of space, was then obtained as $\lambda = 2\mu\nu/(1 - 2\nu)$. The compressible neo-Hookean material model (4) was used.

Fluid model

We used a Reynolds number of 3000 based on the average glottis height $D_g = 0.004$ m and an assumed average velocity in the glottis of $U_m = 40$ m/s. We used these particular values in order to be able to compare with previously published results by Zhao *et al.* [34, 32] and by ourselves [13, 14]. The Prandtl number was set to 1.0, and the Mach number was 0.2, based on the assumed average velocity and the speed of sound. We deliberately used a lower value for the speed of sound, $c_0 = 200$ m/s in order to speed up the computations. The air density was 1.3 kg/m³ and the atmospheric pressure was $p_{\text{atm}} = 101325$ Pa. The equation of state was the perfect gas law, and we assumed a Newtonian fluid. At the inlet, we imposed the acoustic pressure $p_{\text{acoustic}} = p - p_{\text{atm}} = 2736$ Pa, a typical lung pressure during phonation. The outlet pressure was set to atmospheric pressure, i.e. $p - p_{\text{atm}} = 0$ Pa.

If we would not impose any asymmetry in the system, the solution should be symmetric with respect to the centerline at all times. However, this symmetric flow field is not stable, i.e. a small perturbation on one side would cause an asymmetry to build up and never go away (this was seen in our numerical experiments). Also, since the flow is not symmetric in nature, we chose to impose a non-symmetric pressure profile at the inlet by multiplying the given inlet acoustic pressure $p - p_{\text{atm}}$ with a space varying factor $(1 + 0.025 \sin(2\pi\eta))$ where η is a coordinate going from $\eta = 0$ at the lower boundary to $\eta = 1$ at the top boundary.

¹ $\mu(\eta) = \mu_{\text{average}} + \Delta\mu \tanh(-4.5(\eta - 0.5))$, where $\mu_{\text{average}} = (\mu_l + \mu_c)/2$, $\Delta\mu = (\mu_l - \mu_c)/2$ and η is a coordinate going from 0 in the ligament to 1 in the cover.

Numerical simulation

The computational domain is shown in figure 6 with the fluid domain in the middle, between the two independent structure domains. The inflow boundary is to the left and the outflow is to the right. The part of the fluid boundary that is not in contact with the structure is a fixed no-slip adiabatic wall. The fluid-structure interface is a no-slip adiabatic wall which is allowed to deform due to the structure motion.

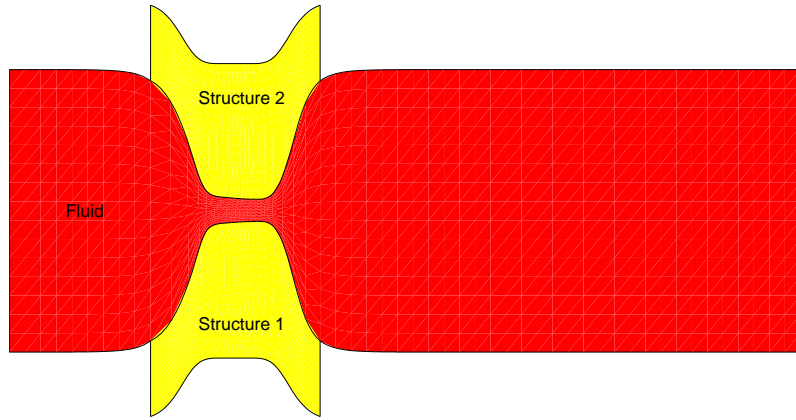


Figure 6: Sketch showing the computational domain for the fluid and the two structure domains.

Both fluid and structure used the same set of variables for nondimensionalization and the same time step was used for both fields so that the two solutions are always at the same time level. The structure grid consisted of 81×61 points for each vocal fold, i.e. for the upper and the lower vocal folds, and the fluid domain was 241×61 points. The time step was determined by the stability condition for the fluid discussed above, which was satisfied here by requiring $CFL \leq 1$. Since the fluid domain changes with time, the CFL condition puts a stricter constraint on the time step when the glottis is nearly closed. The solution was marched in time with given initial and boundary conditions to dimensional time $t = 20$ ms or 416948 time steps, implying an average dimensional time step of $\Delta t = 48$ ns.

Figures 7 and 8 show results for the vorticity and pressure at certain time instants. Initially, the flow is symmetric with two start-up vortices followed by an elongated vortical structure on each side of the centerline. After the start-up vortices leave the domain, the elongated structure becomes unstable and breaks up into smaller circular vortices. As expected, the pressure is lowest inside the vortices. The observed frequency of the oscillation is about 80 Hz, which is close to the typical frequencies that occur in phonation, i.e. 100 Hz for men and 200 Hz for women.

Conclusions

A solver for structural dynamics has been developed using a high order finite difference method to simulate the behavior of biological tissues. This new structural solver has been coupled to an existing compressible flow solver to simulate the fluid-structure interaction that occurs during phonation. The key features of this approach are high order differencing schemes on structured grids and matching grid points at the interface. The structural solver is verified with respect to a test case using the method of manufactured solution and by comparison with a commercial software package.

Our 2D model for the vocal folds and the air flow in the vocal tract proves to be able to capture

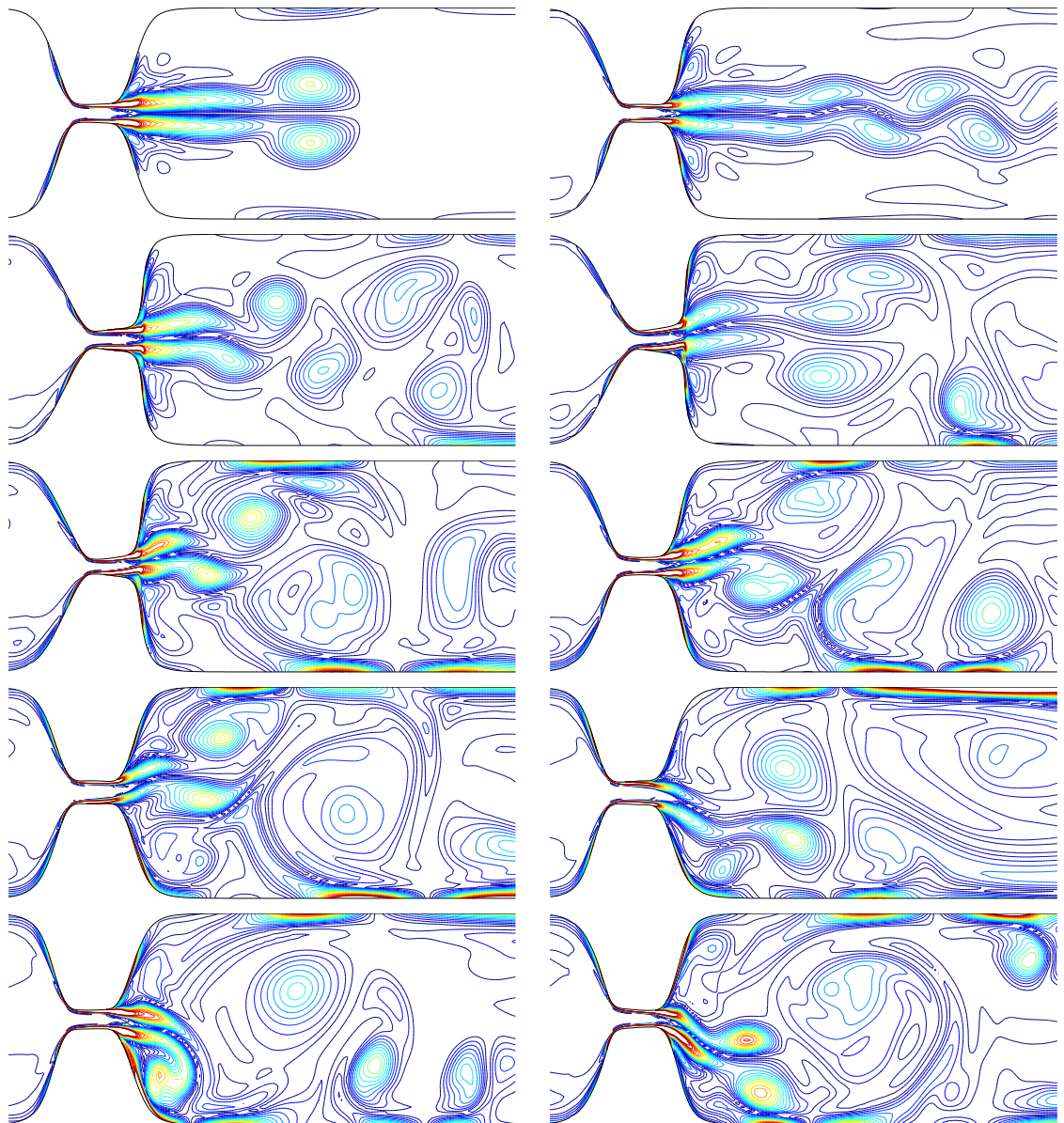


Figure 7: Vorticity contours at 2 ms intervals. Top left subplot is the vorticity at $t = 2$ ms, top right is at $t = 4$ ms and so on up to $t = 20$ ms (lower right). There are 20 equally spaced contour lines between $\omega = 0 \text{ s}^{-1}$ and $\omega = 5 \times 10^4 \text{ s}^{-1}$ in each subplot.

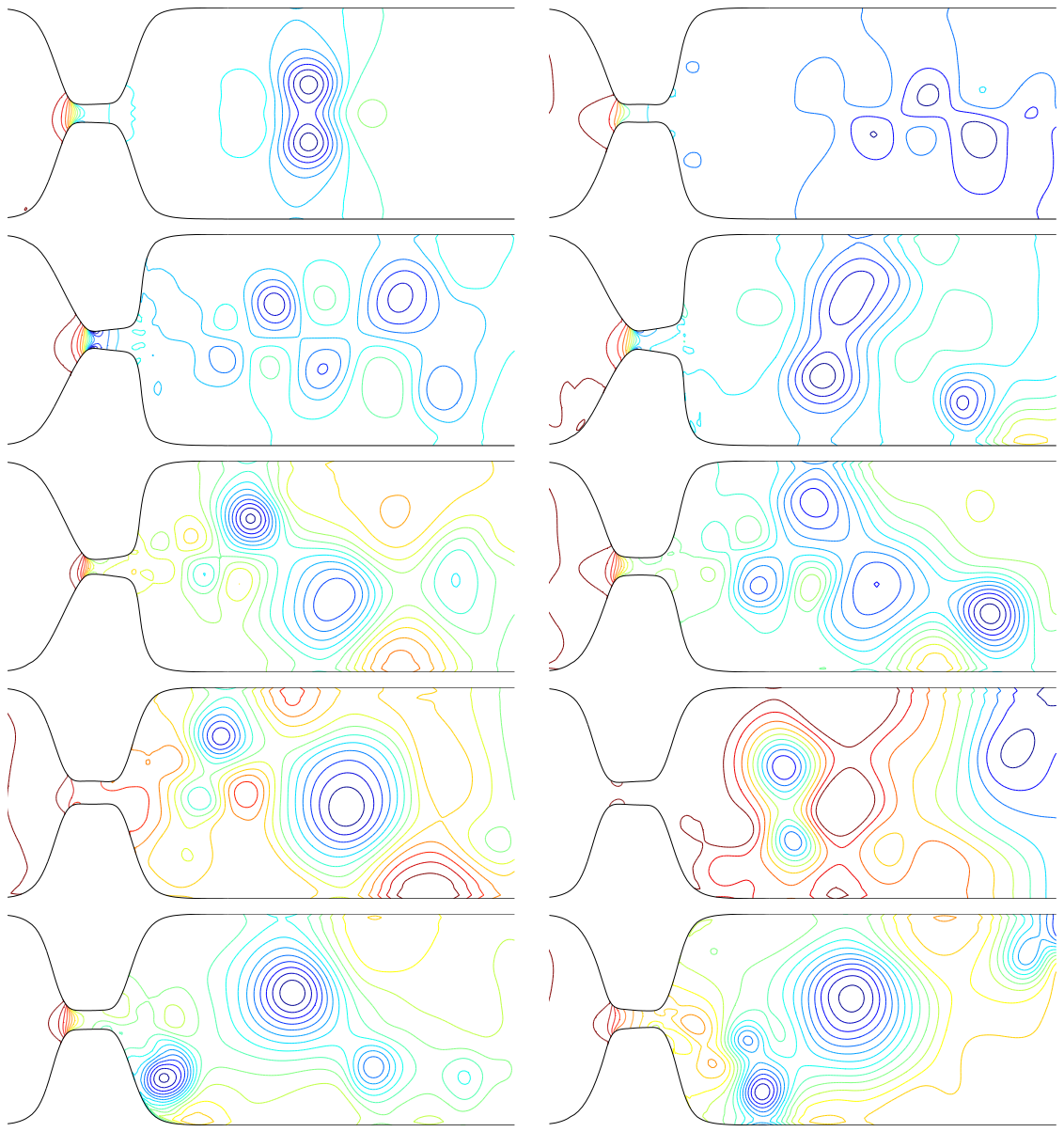


Figure 8: Pressure contours at 2 ms intervals. Top left image is the pressure at $t = 2$ ms, top right is at $t = 4$ ms and so on up to $t = 20$ ms (lower right). There are 20 equally spaced contour lines between $p_{\text{acoustic}} = -3546 \text{ Pa}$ and $p_{\text{acoustic}} = 2837 \text{ Pa}$ in each subplot, where p_{acoustic} is the pressure deviation from the atmospheric pressure, here $p_{\text{atm}} = 101325 \text{ Pa}$ (at the outlet).

the self-sustained pressure-driven oscillations and vortex generation in the glottis. The simulated frequency of 80 Hz is close to 100 Hz, typical for men.

Acknowledgements

The authors thank Bjørn Skallerud, Paul Leinan and Victorien Prot at the Department of Structural Engineering, NTNU for valuable discussions on structure model and Abaqus support. The current research has been funded by the Swedish Research Council under the project "Numerical Simulation of Respiratory Flow".

References

- [1] F. Alipour, D.A. Berry, and I.R. Titze. A finite-element model of vocal-fold vibration. *J. Acoust. Soc. Am.*, 108(6):3003 – 3012, 2000.
- [2] F. Alipour and R.C. Scherer. Vocal fold bulging effects on phonation using a biophysical computer model. *J. Voice*, 14(4):470 – 483, 2000.
- [3] F. Alipour and I.R. Titze. *Combined simulation of two-dimensional airflow and vocal fold vibration*. Ed. P. Davis and N. Fletcher, Singular Publishing Group, San Diego, 1996.
- [4] Dassault Systèmes Simulia Corp., Providence, RI, USA. *Abaqus: Analysis User's Manual, Version 6.8*, 2008.
- [5] J. Degroote, P. Bruggeman, R. Haelterman, and J. Vierendeels. Stability of a coupling technique for partitioned solvers in FSI applications. *Computers and Structures*, 86:2224 – 2234, 2008.
- [6] J.L. Flanagan and L. Landgraf. Self-oscillating source for vocal tract synthesizers. *IEEE Trans. Audio Electroacoust. AU*, 16:57 – 64, 1968.
- [7] J.B. Grotberg and O.E. Jensen. Biofluid mechanics in flexible tubes. *Annu. Rev. Fluid Mech.*, 36:121 – 147, 2004.
- [8] B. Gustafsson. *High order difference methods for time-dependent PDE*. Springer-Verlag Berlin Heidelberg, 2008.
- [9] B. Gustafsson, H.-O. Kreiss, and J. Oliger. *Time Dependent Problems and Difference Methods*. John Wiley & Sons, New York, 1995.
- [10] E.J. Hunter, I.R. Titze, and F. Alipour. A three-dimensional model of vocal fold abduction/adduction. *J. Acoust. Soc. Am.*, 115(4), 2004.
- [11] K. Kormann and M. Kronbichler. High order finite difference approximations for parabolic and hyperbolic-parabolic problems with variable coefficients. Project report, Department of Information Technology, Uppsala University, 2006.
- [12] H.O. Kreiss and L. Wu. On the stability definition of difference approximations for the initial boundary value problem. *Applied Numer. Math.*, 12:213 – 227, 1993.
- [13] M. Larsson. Numerical Simulation of Human Phonation, Master Thesis, Uppsala University, Department of Information Technology, 2007.
- [14] M. Larsson and B. Müller. Numerical simulation of confined pulsating jets in human phonation. *Computers & Fluids*, In Press, 2008.
- [15] H. Luo, R. Mittal, X. Zheng, S.A. Bielamowicz, R.J. Walsh, and J.K. Hahn. An immersed-boundary method for flow - structure interaction in biological systems with application to phonation. *Journal of Computational Physics*, 227:9303 – 9332, 2008.

- [16] K. Mattsson and J. Nordström. Finite difference approximations of second derivatives on summation by parts form. *J. Comput. Physics*, 199:503 – 540, 2004.
- [17] B. Müller. Linear stability condition for explicit Runge–Kutta methods to solve the compressible Navier–Stokes equations. *Mathematical Methods in the Applied Sciences*, 12:139 – 151, 1990.
- [18] B. Müller. Computation of compressible low Mach number flow, Habilitation Thesis, ETH Zürich, 1996.
- [19] B. Müller. High order numerical simulation of aeolian tones. *Computers & Fluids*, 37(4):450 – 462, 2008.
- [20] R.W. Ogden. *Non-linear elastic deformations*. Ellis Horwood Limited, 1984.
- [21] R.W. Ogden. Nonlinear elasticity and fibrous structure in arterial wall mechanics. Lecture Notes for Summer School on Modeling and Computation in Biomechanics held at Graz University of Technology, Austria, 2008.
- [22] T.J. Poinsot and S.K. Lele. Boundary conditions for direct simulations of compressible viscous flows. *J. Comput. Physics*, 101:104 – 129, 1992.
- [23] M. De Oliveira Rosa, J.C. Pereira, M. Grellet, and A. Alwan. A contribution to simulating a three-dimensional larynx model using the finite element method. *J. Acoust. Soc. Am.*, 114:2893 – 2905, 2003.
- [24] D.H. Rudy and J.C. Strikwerda. A nonreflecting outflow boundary condition for subsonic Navier–Stokes calculations. *J. Comput. Physics*, 36:55 – 70, 1980.
- [25] J. Sesterhenn, B. Müller, and H. Thomann. On the cancellation problem in calculating compressible low Mach number flows. *J. Comput. Physics*, 151:597 – 615, 1999.
- [26] P. Šidlof. *Fluid-Structure interaction in human vocal folds*. PhD thesis, Charles University, Prague, 2007.
- [27] B.H. Story and I.R. Titze. Voice simulation with a body-cover model of the vocal folds. *J. Acoust. Soc. Am.*, 97:1249 – 1260, 1995.
- [28] B. Strand. Summation by parts for finite difference approximations for d/dx. *J. Comput. Physics*, 110:47 – 67, 1994.
- [29] I.R. Titze. The human vocal cords: A mathematical model. Part I. *Phonetica*, 28:129 – 170, 1973.
- [30] M.R. Visbal and D.V. Gaitonde. On the use of higher-order finite-difference schemes on curvilinear and deforming meshes. *J. Computat. Physics*, 181:155 – 185, 2002.
- [31] M. Wang, J.B. Freund, and S.K. Lele. Computational prediction of flow-generated sound. *Annu. Rev. Fluid Mech.*, 38:483 – 512, 2006.
- [32] C. Zhang, W. Zhao, S.H. Frankel, and L. Mongeau. Computational aeroacoustics of phonation, Part II: Effects of flow parameters and ventricular folds. *J. Acoust. Soc. Am.*, 112(5):2147 – 2154, 2002.
- [33] W. Zhao, S.H. Frankel, and L. Mongeau. Numerical simulations of sound from confined pulsating axisymmetric jets. *AIAA Journal*, 39(10):1868 – 1874, 2001.
- [34] W. Zhao, S.H. Frankel, and L. Mongeau. Computational aeroacoustics of phonation, Part I: Computational methods and sound generation mechanisms. *J. Acoust. Soc. Am.*, 112(5):2134 – 2146, 2002.
- [35] R.J. Zwaan and B.B. Prananta. Fluid/structure interaction in numerical aeroelastic simulation. *Int. J. Non-Linear Mech.*, 37:987 – 1002, 2002.